Journal of Cranio-Maxillo-Facial Surgery 48 (2020) 105–110

Contents lists available at ScienceDirect

Journal of Cranio-Maxillo-Facial Surgery

journal homepage: www.jcmfs.com

MR imaging as a precise technique to evaluate skull-base tumor volume: Comparison of CT, MR imaging and FDG PET from murine and clinical data

Qing-Xiang Li [a, b, c, d, 1], Rong Yang [a, b, c, d, 1], Yi-Fei Wang [a, b, c, d], Hong-Fang Sun [e], Hai-Bo Wang [f], Hao Liu [b, c, d, g, ***], Yu-Xing Guo [a, b, c, d, **], Chuan-Bin Guo [a, b, c, d, *]

[a] Department of Oral and Maxillofacial Surgery, Peking University School and Hospital of Stomatology, Beijing, 100081, PR China
[b] National Clinical Research Center for Oral Diseases, Beijing, 100081, PR China
[c] National Engineering Laboratory for Digital and Material Technology of Stomatology, Beijing, 100081, PR China
[d] Beijing Key Laboratory of Digital Stomatology, Peking University School and Hospital of Stomatology, Beijing, 100081, PR China
[e] Department of Biomedical Engineering, College of Engineering, Peking University, Beijing, 100871, PR China
[f] Peking University Clinical Research Institute, Beijing, 100191, PR China
[g] The Central Laboratory, Peking University School and Hospital of Stomatology, Beijing, 100081, PR China

ARTICLE INFO

Article history:
Paper received 26 August 2019
Accepted 5 December 2019
Available online 13 December 2019

Keywords:
Skull-base tumor
Multimodal imaging
Animal model
MR imaging

ABSTRACT

In spite of the many imaging modalities used in clinics, the one that best reflects the true delineation of skull-base (infratemporal fossa, ITF) malignancies is still unknown. In order to compare the tumor recognition capabilities of different imaging modalities, established murine models and patients with skull-base tumors were evaluated by computer tomography (CT), magnetic resonance (MR) imaging, and fluorine-18 fluorodeoxyglucose (^{18}FDG) positron emission tomography (PET) for delineation of gross tumor volume (GTV).

PET, MR imaging, and CT enhanced by iodine staining were all sensitive to, and able to recognize, the skull-base tumor in the murine model. No significant difference ($p > 0.9999$) was observed between average GTV according to MR imaging (176.67 ± 19.6 mm^3) and the histological measurement result (170.23 ± 22.24 mm^3) for the murine model. In contrast, the GTVs according to CT (88.77 ± 13.03 mm^3, $p < 0.0001$) and ^{18}FDG PET (35.67 ± 6.56 mm^3, $p < 0.0001$) were much smaller.

In nine patients for whom the three modalities were available, tumor volume comparisons tended to be consistent with the murine model data. According to both the established murine model and clinical patient data, MR imaging possessed the optimal ability to recognize tumor contours.

1. Introduction

The human skull comprises the neurocranium and facial skeleton. The skull base forms the floor of the cranial cavity and separates the brain from other facial structures (Jin et al., 2016). The skull base can be divided into the anterior, middle, and posterior regions (Francies et al., 2018). The complexity of this anatomical site poses surgical challenges to neurosurgeons, otolaryngologists, head-and-neck surgeons, and maxillofacial surgeons alike. The rapid development of imaging technology, along with advanced digitally aided surgical techniques, such as navigation technology and/or robotic surgery, have led to great advances in the treatment of skull-base tumors (Guo et al., 2015a; Zhu et al., 2017).

Various types of tumor occur on the lateral side of the middle skull (infratemporal fossa, ITF), with treatment carrying a high risk of injuring vital neurovascular structures (IX-XII cranial nerves, internal carotid artery, and internal jugular vein) (Guo et al., 2015a; DePowell et al., 2014). Many different approaches can be used to

* Corresponding author. 22 Zhongguancun Nandajie Haidian District, Beijing, 100081, PR China. Fax: +86 10 62173402.
** Corresponding author. 22 Zhongguancun Nandajie Haidian District, Beijing, 100081, PR China. Fax: +86 10 62173402.
*** Corresponding author. 22 Zhongguancun Nandajie Haidian District, Beijing, 100081, PR China. Fax: +86 10 62173402.
E-mail addresses: liqingxiang1992@126.com (Q.-X. Li), yrpkuhsc2011@163.com (R. Yang), sdu2003@126.com (H. Liu), gladiater1984@163.com (Y.-X. Guo), chuanbinguo@126.com (C.-B. Guo).
[1] First author.

https://doi.org/10.1016/j.jcms.2019.12.007
1010-5182/

reach this space during surgery, but these often need incisions in the face (Sanna et al., 2014; Guo and Guo, 2014). As unsettling as this sounds, it is often necessary in order to reach the skull base and treat the problem that is present. Endoscopic surgery is sometimes chosen to avoid any external incision and it is considered to be 'minimally invasive' (Giovannetti et al., 2018; Gras-Cabrerizo et al., 2013). When a malignant tumor is adjacent to the vital neurovascular structures referred to above, it is difficult to achieve a clear surgical margin.

Supplementary postoperative treatment, such as stereotactic radiotherapy, could help enhance the treatment of skull-base malignancies. Advanced image-guided software can help to precisely locate a hard-to-reach skull-base tumor in order to administer a small, highly targeted dose of radiation to slow the growth of the tumor, without affecting nearby healthy tissues (Fossati et al., 2016). But it is hard to distinguish the remaining tumor from surrounding normal tissues in postoperative and/or patients with recurrence due to structure distortion (Guo et al., 2015b). In addition, the residual metal hemostatic clips or brachytherapy seeds in the surgical field will cause artifacts in postoperative computed tomography (CT) images, which can influence decisions regarding future radiotherapy (Dolati et al., 2015; Valentino et al., 1991).

CT, magnetic resonance (MR) imaging, and fluorine-18 fluorodeoxyglucose (FDG) positron emission tomography (PET) are frequently used to evaluate recurrent skull-base tumors (Daisne et al., 2004). Multimodality imaging fusion technology was applied to deal with the above problems in our clinical work. With the same coordinate system, the tumor contours indicated by different modalities were not often consistent with each other, but which modality was the most optimal one for skull-base tumor contour recognition remained unclear.

In order to evaluate the role of different imaging techniques in the recognition of skull-base tumors, a murine model with skull-base tumor was established. We found that ultrasound when combined with fluorescence was effective during tumor cell transplantation, and also to ascertain successful model establishment. Multiple imaging methods, such as CT, MR imaging, and PET, were used to confirm the skull-base tumor formation. Finally, histology-based gross tumor volume (GTV) measurements were used to compare the recognition abilities of the three imaging modalities.

2. Materials and methods

2.1. Mice

A total of six female BALB/c nude mice (4–5 weeks old; 12–14 g) were supplied by Beijing Vital River Laboratories. All mice were housed under standard conditions in the animal facility of Peking University Hospital and School of Stomatology (PKUSS). All procedures were performed according to the Peking University Health Science Center Animal Research Committee-approved protocol (LA2018247). All mice were accustomed to their new surroundings for 1 week prior to the start of the experiment.

2.2. Cell culture

WSU-HN-6-line human squamous cell carcinoma (SCC) cells were first cultured and immortalized from human tongue SCC at Wayne State University (Cardinali et al., 1995). All cells were cultured in DMEM (Gibco, Rockville, MD, USA) containing 10% (v/v) FBS (HyClone, Logan, UT, USA), 100 U/ml of penicillin, and 100 mg/ml streptomycin at 37 °C, in a humidified atmosphere with 5% CO_2 (Kim et al., 1997).

2.3. Generation of HN-6 cell line with expression of green fluorescent protein (GFP)

For GFP gene transduction, 20% confluent HN-6 cells were incubated with GFP-lentivirus supernatants from the 293T packaging cells for 72 h. High GFP-expression cell clones were selected by puromycin (Selleck Chemical, Houston, TX, USA). Cell clones were visualized by fluorescence microscopy to detect GFP.

2.4. Animal experiment

The skull-base tumor animal model was induced by injection of WSU-HN-6-GFP cell lines via a submandibular approach. A total of 2×10^5 HN-6 cells in 20 μL PBS were implanted in nude mice by stereotaxic injection into the ITF space. The procedure was carried out under ultrasonographic guidance (VisualSonics Vevo® 1100) (Supplementary Figure 1).

2.5. Primary assessment of animal model

All animals were screened by ultrasonography and fluorescence detection once a week after the cell injection, until their euthanasia 3 weeks later via carbon dioxide overdose and cervical dislocation. A prewarmed ultrasound gel (Aquasonic, Parker Laboratories, Fairfield, NJ, USA) was applied to the skin of submandibular area to facilitate sound transmission and to reduce contact artifacts. The potential tumor was visualized using a 40 MHz ultrasound probe. All mice underwent *in vivo* imaging in a supine position using an IVIS® Spectrum *in vivo* system (PerkinElmer Inc., Waltham, MA, USA). The system captured fluorescent light in targeted organs using GFP filter sets with an excitation wavelength of 480 nm, and emission wavelength of 520 nm. Imaging data were recorded and analyzed using the Living Imaging 4.4 software package (PerkinElmer Inc).

2.6. Imaging assessment for the animal model

Six mice underwent live scanning with MR imaging and PET/CT under anesthesia. Post-euthanasia CT scanning was carried out on all fixed head specimens before and after 4 days of 3.75% Lugol's iodine staining.

2.7. Living MR imaging and PET/CT analysis

For MR imaging and PET, mice were anesthetized with 2–3% isoflurane mixed in oxygen. Mice were placed in a supine position, lying on an adjustable platform. A Bruker 94/20 9.4T (Bruker, Ettingen, Germany) MR imaging system was used. Gradient strength was 660 mTm^{-1}. MR imaging was performed with a gradient echo sequence with the following parameters: TE 10 ms, TR 200 ms, flip angle 70°, receiver bandwidth 52 Hz per pixel, echo-shift to 25% of readout period, FOV 26 × 26 × 16 mm, matrix size 64 × 64 × 16 mm, actual spatial resolution 410 × 410 × 1000 mm (Massot et al., 2012).

During the PET/CT examination procedure, a heparin-coated catheter was placed in the tail vein for free-radical injection. 500 uci/mice ^{18}F-FDG in 100 μL saline was manually injected for 60 min prior to the 15 min' static scanning acquisition with an Inveon PET scanner (Siemens, Germany). The PET images were corrected for attenuation, scatter, normalization, and camera dead time, and coregistered with CT images. The tumor uptake of 18F-FDG and volume measurement were calculated in terms of the standardized uptake value (SUV) in the three-dimensional regions of interest (ROIs) (Su et al., 2018). Mice were then euthanized immediately

after PET scanning, and immersed in 4% paraformaldehyde overnight for the following analysis.

2.8. Post-euthanasia CT analysis

Intact skulls were dissected and stained with 3.75% Lugol's iodine solution for 4 days (Jeffery et al., 2011). Samples were radiographed using a CT device (Inveon MM Gantry-STD, Siemens, Germany) in the PKUSS Imaging Center. Images were collected at a resolution of 9 μm using 60 kVp and 220 μA for the X-ray source.

2.9. Histology

Following decalcification in 20% EDTA for 2–4 weeks, samples were passed through serial concentrations of ethanol for paraffin embedding. After sectioning into 9–10 μm slices using a microtome (Leica), hematoxylin and eosin (H-E) staining and Pan-Keratin (1:1000, Proteintech Group, Inc, Rosemont, PA, USA) immunohistochemical (IHC) staining were carried out in deparaffinized sections following standard procedures. Bright-field microscopy and stereomicroscopy (Leica) were used to visualize and capture the serial axial views of the skull-base tumor.

2.10. Patient selection

The study was approved by the Institutional Biomedicine Ethics Committee of PKUSS (PKUSSIRB-2013039). Nine patients with malignant tumors of the ITF were included in the study after obtaining their informed consent. All patients underwent contrast CT, MR imaging, and FDG PET within a 2-day period.

2.11. Delineation of gross tumor volume (GTV)

CT, MR, and FDG-PET imaging data from the murine model were recorded in DICOM format and imported into iPlan software (Brainlab) to perform delineation of GTV. For CT, GTVs were delineated from images with fixed-display window settings (center 0 HU, width 300 HU). For MR imaging, GTVs were initially determined from the T2-weighted images. For PET, GTVs were delineated automatically using a segmentation algorithm based on the measured signal-to-noise ratio (Daisne et al., 2004).

For the patients' imaging data, GTVs were determined from three-dimensional visualization of gross tumor infiltration on the iPlan software. One section in five was captured by stereoscope, and tumor volume calculated using outline sizes in ImageJ 6.0 software. Tumor volume was calculated using the formula $V = (W^2 \times L)/2$ (Faustino-Rocha et al., 2013). This approach was then used to compare volumes ascertained with the different imaging methods.

2.12. Statistics

The GTVs obtained from CT, MR, PET, and histological specimen images were compared firstly using one-way ANOVA analysis to determine significance for the different pairs of imaging modalities. When the statistical results were significantly different ($p < 0.05$), GTVs from CT, MR, and PET were compared with the histological results again. Adjustments for multiple comparisons were made using Tukey's method (0.05/3). The patients' GTVs obtained from CT, MR, and PET were analyzed in the same way. All statistical calculations were performed with Graphpad Prism (version 7.0). A p-value < 0.05 was considered to represent a significant difference. Statistical data were presented as mean ± SD. Qualitative analysis (Q.X.L, R.Y, Y.X.G) of GTVs was also performed for all imaging modalities and for the macroscopic specimens.

3. Results

3.1. Primary assessment of animal model

Non-traumatic ultrasonography and *in vivo* fluorescence imaging methods were used to confirm skull-base tumor formation in all animals. An obvious asymmetrical appearance was detected via ultrasonography 3 weeks after tumor cell injection. It was harder to distinguish the cervical vessels on the right-hand, tumor-cell-injection side compared with the non-treatment left-hand side (Supplementary Figure 2A). Fluorescence imaging also showed bright signals close to the right submandibular area, whereas no signal was found on the left side (Supplementary Figure 2B).

3.2. CT, MR imaging, and PET analysis of animal model

Original CT data were imported using iPlan software for imaging analysis. CT was easily able to indicate bone invasion of the skull base, but could not indicate tumor location before Lugol's iodine staining (Supplementary Figure 3). After iodine staining, the skull-base tumor could be easily recognized from the surrounding muscles (Fig. 1A, B).

The advantage of MR imaging for displaying soft tissue was demonstrated clearly when compared with stained CT imaging. The tumor outline and circumambient muscle or brain tissue could be distinguished during imaging analysis (Fig. 1C, D).

PET was also used to confirm tumor formation in our animal model. Compared with non-treatment control mice, there was an obvious high-metabolism tumor under the brain and eyes (Fig. 1E–H). The tumor outline from PET imaging seemed less extensive than with CT or MR imaging. The mean SUV of the three-dimensional region of interest was around 2.75.

3.3. Tumor volume comparison between different imaging methods

H-E staining data indicated the skull-base tumor formation. In the continuous sections, tumor outlines were clearly detected deep in the masseter muscle and below the skull base (Fig. 2B). Immunohistochemical staining analysis showed that the tumor was epithelial-derived squamous cell carcinoma (Fig. 2C, D).

Tumor volumes according to CT, MR imaging, and PET were calculated with image-analyzing software through continuous outlining of the three-dimensional tumor region or using the high–metabolism activity associated with malignant tumors. For the skull-base tumors, the mean GTV established by MR imaging (176.67 ± 19.6 mm^3) was closer to the reference value derived from H-E-stained slide measurements (170.23 ± 22.24 mm^3, $p > 0.9999$), while GTVs from CT and PET were significantly different from the histological results (88.77 ± 13.03 mm^3 [$p < 0.0001$] and 35.67 ± 6.56 mm^3 [$p < 0.0001$], respectively) (Fig. 2E).

3.4. Comparison of tumor recognition ability of different imaging techniques in clinical patients

Nine cases of malignant tumor invasion into the ITF were preoperatively evaluated using contrast CT, MR imaging, and PET examination. The imaging data were imported into iPlan software, and merged into the same coordinate system. In case No.1, MR imaging was able to indicate tumor contours more clearly and precisely than contrast CT or PET. Tumor volumes for the same patient in descending order of size were established by MR imaging, CT, and PET. The maxillary tuberosity showed clear signs of bone invasion in MR imaging, but seemed normal in contrast CT. While PET only indicated high-metabolism regions, a much reduced tumor contour was observed than with CT and MR imaging

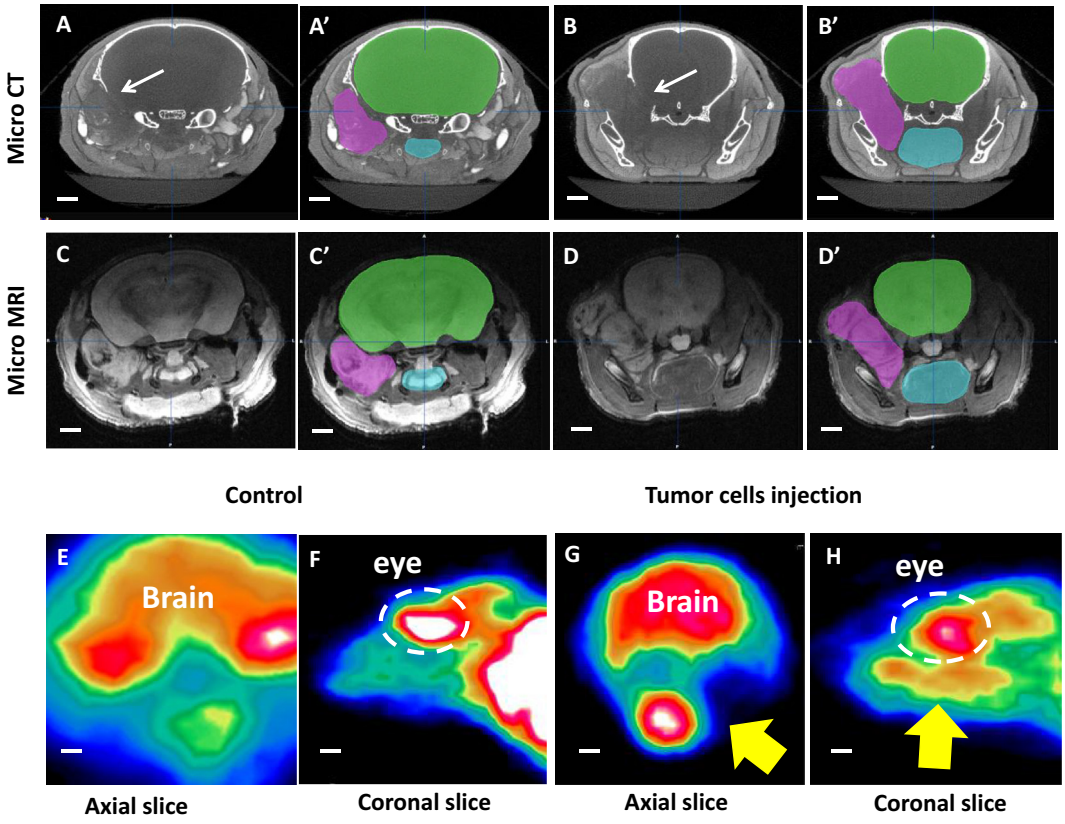

Fig. 1. CT (stained) and MR imaging indicating tumor formation below the skull base. (A–B) Stained CT showing tumor formation and bone invasion (indicated by white arrows). (C–D) MR imaging showing tumor formation located close to the brain. The tumor, brain and tongue was labeled as purple, green and blue color respectively. (E–H) Representative PET images of the murine model, with the skull base tumor indicated by yellow arrows. The dotted circles indicate location of the eyes. Scale bars = 1 mm.

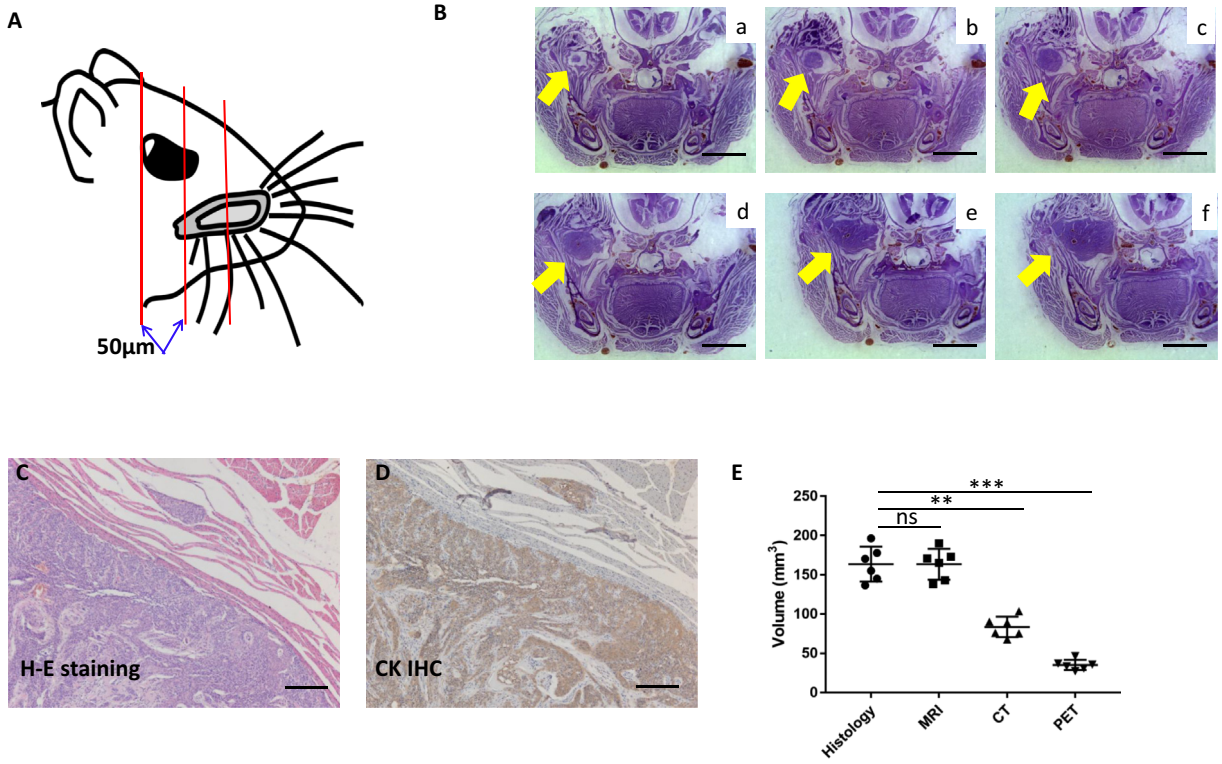

Fig. 2. Tumor volume calculation based on continuous histological sections. (A–B) Schematic drawing of section orientation for a murine skull-base tumor model. Continuous sections captured by stereomicroscope at 50 μm intervals. (C–D) H-E and Pan-Keratin IHC staining to confirm presence of squamous cell carcinoma. (E) Quantification of GTVs from histological sections and different imaging methods. ns no significance; $^{***}p < 0.001$. Comparison of the histological result with MR imaging, CT, and PET gave p-values of >0.9999, <0.0001, and 0.001, respectively. Scale bars in B = 2 mm; scale bars in C and D = 200 μm.

data (Fig. 3A–I). Tumor volume comparisions showed MR imaging to be more sensitive in the delineation of skull-base (ITF) malignancies (Table 1 and Fig. 3J).

4. Discussion

While skull-base tumors offer many challenges in a clinical setting, there is no optimal animal model used to investigate their biological behavior (Jarrahy et al., 1999; Vora, 2017). In our previous investigation, the pathological types of ITF malignant tumor were widely varied, with squamous cell carcinoma accounting for nearly one third of cases. For a skull-base tumor, knowing its correct location and its relationship with surrounding vital vessels could help to guarantee safe, micro-invasive surgery (Blake et al., 2014; Iida and Anzai, 2017). Furthermore, many cases of skull-base malignancies that are not resected with safe margins need post-operative adjuvant radiotherapy to obtain better control of tumor growth (Johnson and Barani, 2013). Therefore, understanding the properties of different imaging methods in detecting tumor contours requires thorough exploration.

Our skull-base tumor murine model successfully mimicked a clinically common tumor type. Ultrasonographic guidance reduced the risk of cervical vessel injury when transferring tumor cells into the ITF space. Moreover, ultrasonography and *in vivo* fluorescence

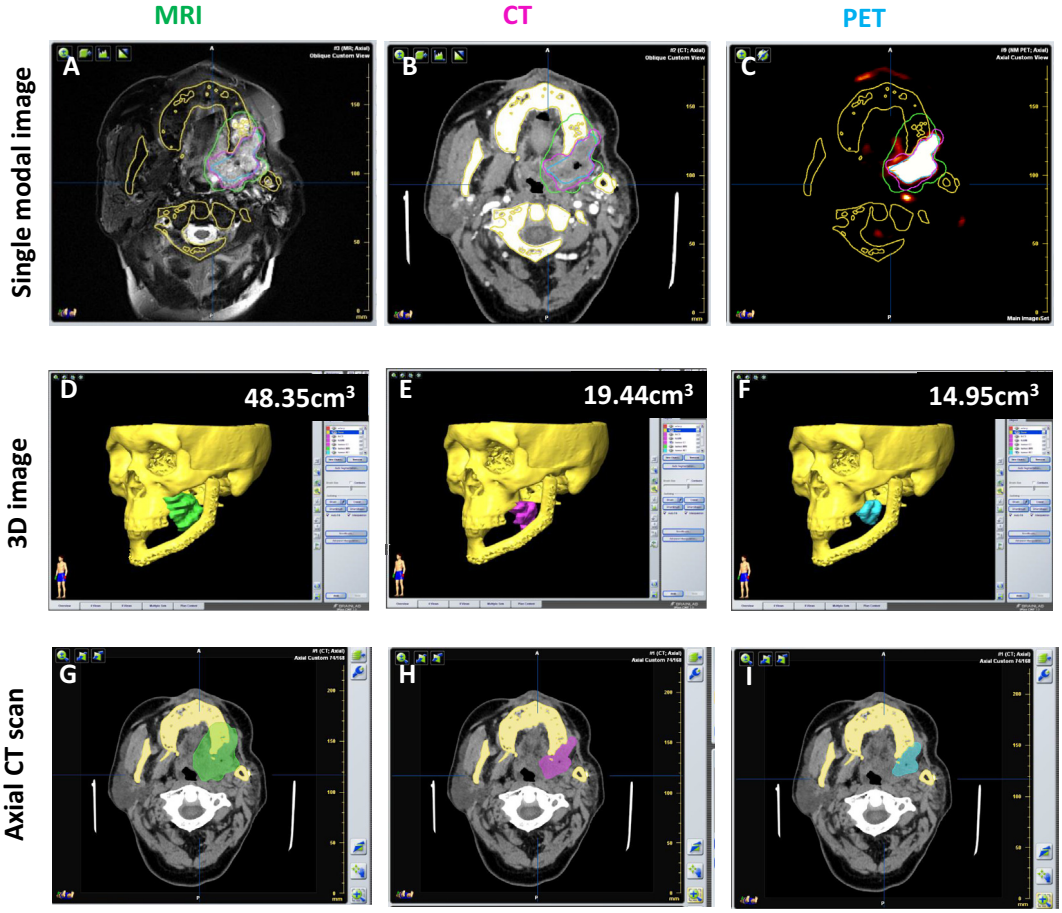

Fig. 3. Tumor volume comparision for case 1, with infratemporal fossa malignancies monitored by contrast CT, MR imaging, and PET. (A–C) The tumor is indicated in green (contrast CT), purple (MR imaging), and blue (PET), using imaging data based on the same coordinate system. (D–I) Tumor counters derived from contrast CT, MR imaging, and PET data displayed in 3D image and axial CT image form. GTVs for case 1 calculated from different imaging data are labeled in Figures D–F.

Table 1
Summary of patient data.

Patient No./age/sex	Primary or recurrent	Histological findings	GTV-MRI (cm^3)	GTV-CT (cm^3)	GTV-PET (cm^3)
1/54/male	Recurrent	SCC	48.35	19.44	14.95
2/45/male	Recurrent	SCC	44.14	3.94	5.20
3/54/male	Primary	SCC	33.43	17.73	18.29
4/63/male	Primary	SCC	30.60	22.11	17.64
5/53/male	Recurrent	Rhabdomyosarcoma	38.01	20.77	19.65
6/66/male	Recurrent	ACC	6.97	3.33	4.52
7/47/male	Recurrent	Synovial sarcoma	70.33	67.41	26.60
8/9/female	Recurrent	Rhabdomyosarcoma	18.64	4.78	7.78
9/6/male	Recurrent	PNET	16.46	6.05	5.14
Mean			34.1	18.39	13.31*

SCC, squamous cell carcinoma; ACC, adenoid cystic carcinoma; PNET, primitive neuroectodermal tumor.
*ANOVA analysis of GTVs for nine cases with MRI and CT; $p = 0.0358$ and $p = 0.7946$, respectively.

imaging allowed non-invasive determination of whether the tumor had formed in each model animal. Once tumor formation was confirmed, several model imaging methods (live MR imaging, PET scans, and stained CT scans) were used to evaluate tumor growth. The objective appraisal of different imaging methods for tumor volume evaluation for all malignancies was achieved through comparison with the gold-standard value generated by H-E and Pan-Keratin IHC staining analysis (Ayers et al., 2010; Cavalcanti et al., 2004). As a consequence, MR imaging was found to be the most sensitive method for ascertaining gross tumor volume, while CT helped the assessment of bone changes (Ramasawmy et al., 2016; Thust and Yousry, 2016). The glucose metabolic changes in skull-base malignancies highlighted by PET were not uniform, and so could not accurately represent the real scope of tumor invasion. These specific characteristics of the different imaging methods were also demonstrated in our clinical cases.

A major finding of our study, which could have tremendous implications for navigation-guided surgery and radiation therapy treatment planning in patients with skull-base malignancies, was that the GTVs delineated at MR imaging were by far the closest to the reference values calculated from histological specimens. It is suggested that when the surgical resection of malignant skull-base tumors is planned, then MR imaging combined with CT examination is recommended. PET is important in judging the nature of malignant tumors and the extent of systemic metastasis. However, it is not suitable for tumor evaluation in terms of quantitative and locational characteristics.

This study has some limitations that need to be pointed out. The observation samples were not very large in both the animal and clinical studies. Further prospective clinical studies with larger sample sizes and longer follow-up terms are necessary.

5. Conclusion

In summary, an animal model for skull-base malignancy was successfully established using our method. After verification and evaluation with various imaging methods, the potential role of MR imaging for the delineation of GTV in skull-base malignancies has been demonstrated. The efficacy of this modality on the delineation of the surgical target could help in designing the surgical strategy for full removal of skull-base tumors, and reduce the possibility of recurrence. The impact of this conclusion on radiation dose allocation requires further evaluation.

Funding

This work was supported by the Beijing Municipal Science and Technology Commission [Z161100000516043], the Beijing Natural Science Foundation [7162113], and the National Natural Science Foundation of China [81672664, 81700935, 81900979].

Appendix A. Supplementary data

Supplementary data to this article can be found online at https://doi.org/10.1016/j.jcms.2019.12.007.

References

Ayers GD, McKinley ET, Zhao P, Fritz JM, Metry RE, Deal BC, et al: Volume of preclinical xenograft tumors is more accurately assessed by ultrasound imaging than manual caliper measurements. J Ultrasound Med 29(6): 891–901, 2010

Blake DM, Husain Q, Kanumuri VV, Svider PF, Eloy JA, Liu JK: Endoscopic endonasal resection of sinonasal and anterior skull base schwannomas. J Clin Neurosci 21(8): 1419–1423, 2014

Cardinali M, Pietraszkiewicz H, Ensley JF, Robbins KC: Tyrosine phosphorylation as a marker for aberrantly regulated growth-promoting pathways in cell lines derived from head and neck malignancies. Int J Cancer 61(1): 98–103, 1995

Cavalcanti MG, Santos DT, Perrella A, Vannier MW: CT-based analysis of malignant tumor volume and localization. A preliminary study. Braz Oral Res 18(4): 338–344, 2004

Daisne J-F, Duprez T, Weynand B, Lonneux M, Hamoir M, Reychler H, et al: Tumor volume in pharyngolaryngeal squamous cell carcinoma: comparison at CT, MR imaging, and FDG PET and validation with surgical specimen. Radiology 233(1): 93–100, 2004

DePowell JJ, Froelich SC, Zimmer LA, Leach JL, Karkas A, Theodosopoulos PV, et al: Segments of the internal carotid artery during endoscopic transnasal and open cranial approaches: can a uniform nomenclature apply to both? World Neurosurg 82(6 Suppl): S66–S71, 2014

Dolati P, Gokoglu A, Eichberg D, Zamani A, Golby A, Al-Mefty O: Multimodal navigated skull base tumor resection using image-based vascular and cranial nerve segmentation: a prospective pilot study. Surg Neurol Int 6: 172, 2015

Faustino-Rocha A, Oliveira PA, Pinho-Oliveira J, Teixeira-Guedes C, Soares-Maia R, da Costa RG, et al: Estimation of rat mammary tumor volume using caliper and ultrasonography measurements. Lab Anim (NY) 42(6): 217–224, 2013

Fossati P, Vavassori A, Deantonio L, Ferrara E, Krengli M, Orecchia R: Review of photon and proton radiotherapy for skull base tumours. Rep Pract Oncol Radiother 21(4): 336–355, 2016

Francies O, Makalanda L, Paraskevopolous D, Adams A: Imaging review of the anterior skull base. Acta Radiol Open 7(5), 2018 2058460118776487

Giovannetti F, Mussa F, Priore P, Scagnet M, Arcovio E, Valentini V, et al: Endoscopic endonasal skull base surgery in pediatric patients. A single center experience. J Craniomaxillofac Surg 46(12), 2018 2017–21

Gras-Cabrerizo JR, Munoz-Hernandez F, Montserrat-Gili JR, Tresserras-Ribo P, de Juan-Delago M, Webb SM, et al: Endoscopic surgery in the skull base unit: experience in the first 72 cases. Acta Otorrinolaringol Esp 64(3): 169–175, 2013

Guo Y, Guo C: Maxillary-fronto-temporal approach for removal of recurrent malignant infratemporal fossa tumors: anatomical and clinical study. J Craniomaxillofac Surg 42(3): 206–212, 2014

Guo YX, Sun ZP, Liu XJ, Bhandari K, Guo CB: Surgical safety distances in the infratemporal fossa: three-dimensional measurement study. Int J Oral Maxillofac Surg 44(5): 555–561, 2015

Guo R, Guo YX, Feng Z, Guo CB: Application of a computer-aided navigation technique in surgery for recurrent malignant infratemporal fossa tumors. J Craniofac Surg 26(2), 2015 e126–32

Iida E, Anzai Y: Imaging of paranasal sinuses and anterior skull base and relevant anatomic variations. Radiol Clin North Am 55(1): 31–52, 2017

Jarrahy R, Young J, Berci G, Shahinian HK: Endoscopic skull base surgery I: a new animal model for pituitary surgery. J Invest Surg 12(5): 289–294, 1999

Jeffery NS, Stephenson RS, Gallagher JA, Jarvis JC, Cox PG: Micro-computed tomography with iodine staining resolves the arrangement of muscle fibres. J Biomech 44(1): 189–192, 2011

Jin SW, Sim KB, Kim SD: Development and growth of the normal cranial vault: an embryologic review. J Korean Neurosurg Soc 59(3): 192–196, 2016

Johnson J, Barani IJ: Radiotherapy for malignant tumors of the skull base. Neurosurg Clin N Am 24(1): 125–135, 2013

Kim SY, Chu KC, Lee HR, Lee KS, Carey TE: Establishment and characterization of nine new head and neck cancer cell lines. Acta Otolaryngol 117(5): 775–784, 1997

Massot P, Parzy E, Pourtau L, Mellet P, Madelin G, Marque S, et al: In vivo high-resolution 3D overhauser-enhanced MRI in mice at 0.2 T. Contrast Media Mol Imaging 7(1): 45–50, 2012

Ramasawmy R, Johnson SP, Roberts TA, Stuckey DJ, David AL, Pedley RB, et al: Monitoring the growth of an orthotopic tumour xenograft model: multi-modal imaging assessment with benchtop MRI (1T), high-field MRI (9.4T), ultrasound and bioluminescence. PLoS One 11(5): e0156162, 2016

Sanna M, Shin SH, Piazza P, Pasanisi E, Vitullo F, Di Lella F, et al: Infratemporal fossa approach type a with transcondylar-transtubercular extension for Fisch type C2 to C4 tympanojugular paragangliomas. Head Neck 36(11): 1581–1588, 2014

Su S, Chen J, Yao H, Liu J, Yu S, Lao L, et al: CD10(+)GPR77(+) cancer-associated fibroblasts promote cancer formation and chemoresistance by sustaining cancer stemness. Cell 172(4): 841–856, 2018 e16

Thust SC, Yousry T: Imaging of skull base tumours. Rep Pract Oncol Radiother 21(4): 304–318, 2016

Valentino DJ, Mazziotta JC, Huang HK: Volume rendering of multimodal images: application to MRI and PET imaging of the human brain. IEEE Trans Med Imaging 10(4): 554–562, 1991

Vora SR: Mouse models for the study of cranial base growth and anomalies. Orthod Craniofac Res 20(Suppl. 1): 18–25, 2017

Zhu JH, Wang J, Wang YG, Li M, Guo YX, Liu XJ, et al: Performance of robotic assistance for skull base biopsy: a phantom study. J Neurol Surg B Skull Base 78(5): 385–392, 2017